Gigahertz Phononic Integrated Circuits Based on Overlay Slot Waveguides

Ziyao Feng[1,†] Yang Liu[2,†] Xiang Xi,[1] Lai Wang[2] and Xiankai Sun[1,*]

[1]*Department of Electronic Engineering, The Chinese University of Hong Kong, Shatin, New Territories, Hong Kong SAR, China*

[2]*Beijing National Research Center for Information Science and Technology (BNRist), Department of Electronic Engineering, Tsinghua University, Beijing 100084, China*

Harnessing the properties of phonons on a chip, phononic integrated circuits are playing an increasingly important role in optoelectronic integration. To date, most of such phononic waveguides are realized by etching a piezoelectric layer and forming a wire, which not only involves complicated fabrication processes but also limits integration with electronic and photonic elements on the same chip. To overcome these difficulties, here we propose and demonstrate a type of overlay slot phononic waveguide obtained by patterning a thin silicon cladding layer on an unetched gallium-nitride-on-sapphire substrate. We experimentally demonstrate the guiding and power splitting of gigahertz surface acoustic waves in such waveguides, with a measured propagation loss of about 1.80 dB/mm for the Rayleigh mode. We also theoretically predict that the Love mode in such waveguides can turn into a phononic bound state in the continuum under special conditions. Such waveguides introduce an alternative paradigm for phononic integrated circuitry and will enable applications in information processing, environmental monitoring, and noninvasive manipulation of biomolecules on a chip.

I. INTRODUCTION

With the development of nanofabrication techniques, nanomechanical devices and systems have attracted wide attention in the past decades [1–3]. They are exploited not only for investigating the fundamental properties of phonons [4,5] but also for studying the interaction between phonons and other degrees of freedom in the classical and quantum regimes, such as environmental monitoring [6–8], quantum state control [9], and quantum communications [10]. However, most nanomechanical systems take the form of suspended structures, and thus suffer from complicated fabrication processes and device fragility. On the other hand, nanomechanical systems based on surface acoustic waves in piezoelectric materials are employed in many applications, such as signal processing [11,12], biomaterial sensing [13], quantum and topological effects [14–16], chemical analysis [17], and noninvasive manipulation of biomolecules [18,19]. In these systems, the nanomechanical structures do not need to be suspended, and thus have improved structural stability [20]. To date, individual phononic components, such as acoustic resonators [21] and lenses [22], have been demonstrated. However, phononic waveguides, which guide and

route acoustic waves between individual components in a phononic integrated circuit, remain less explored.

The concept of acoustic waveguides (i.e., phononic waveguides in the low-frequency regime) was theoretically proposed and experimentally demonstrated about half a century ago [23,24], including the types of overlay strips, topographic ribs, and overlay slot waveguides. Figures 1(b)–1(d) illustrate their cross sections, where the acoustic waves tend to be confined laterally to a material with a lower acoustic velocity v. The immature fabrication techniques and lack of required materials at that time limited their further development. Later, phononic waveguides based on phononic band-gap effects were proposed [25,26], but they required complicated designs to achieve tight confinement of acoustic waves. More recently, the development of nanofabrication techniques enabled suspended phononic waveguides [Fig. 1(a)] that led to suspended coupled resonator arrays [27–29] and suspended wires [30,31]. These waveguides can guide high-frequency acoustic waves with simple designs, but they suffer from fabrication complexity and device fragility due to their suspended nanomechanical structures. To solve these issues, a nonsuspended scheme based on overlay strip waveguides [Fig. 1(b)] was developed on a gallium-nitride-on-sapphire platform, where the phononic waveguides were formed by patterning and etching the gallium nitride (GaN) layer [32–34]. This method requires deep etching of GaN, which
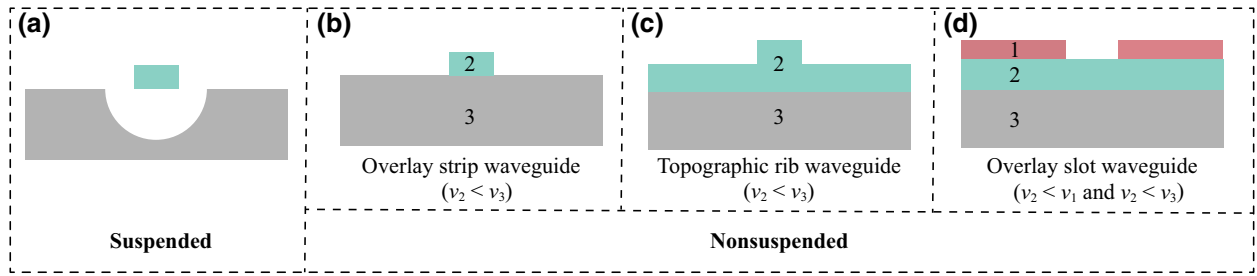
FIG. 1.   Cross-sectional illustrations of suspended (a) and nonsuspended (b)–(d) phononic waveguides. Nonsuspended scheme includes overlay strip (b), topographic rib (c), and overlay slot (d) waveguides.

sets a limitation for the phononic circuits to be integrated with electronic and photonic circuits on the same chip.

To overcome all these challenges, here we propose and experimentally demonstrate an overlay slot phononic waveguide [Fig. 1(d)] by patterning a thin crystalline silicon cladding layer on an unetched GaN-on-sapphire substrate. This structure can laterally confine and longitudinally guide gigahertz acoustic waves with a measured propagation loss of about 1.80 dB/mm for the Rayleigh mode. This propagation loss is comparable to those of fully etched and/or suspended wire waveguides at similar frequencies [31,35]. We further experimentally demonstrate a multimode waveguide for use in power splitting with different splitting ratios. Additionally, we theoretically predict that the Love mode in such waveguides can turn into a phononic bound state in the continuum under special conditions. With simple fabrication processes and enhanced device robustness, such waveguides introduce an alternative paradigm for functional phononic integrated circuitry on a chip.

II. RESULTS

Figure 2(a) illustrates the proposed overlay slot phononic waveguides for gigahertz phononic integrated circuits. A silicon cladding layer (Young's modulus $E = 165$ GPa, mass density $\rho = 2330$ kg/m^3, and Poisson's ratio $\nu = 0.22$) is patterned on a GaN layer ($E = 233$ GPa, $\rho = 6110$ kg/m^3, and $\nu = 0.198$) on a sapphire substrate ($E = 345$ GPa, $\rho = 3980$ kg/m^3, and $\nu = 0.29$). Figure 2(b) shows the cross section of the phononic waveguide and the corresponding cross-sectional distribution of effective velocity of the supported acoustic waves propagating in the longitudinal (y) direction. The thicknesses of the silicon cladding and GaN layers are h_{clad} and h_{GaN}, respectively. This waveguide can support multiple acoustic modes, which are transversely confined and longitudinally guided in the central uncladded region with a width of w, due to the existence of a potential well in the distribution of effective acoustic velocity. There are two types of acoustic modes, namely, the Rayleigh mode [Fig. 2(c)] and the

Love mode [Fig. 2(d)]. The Rayleigh mode vibrates mainly in the vertical (z) direction, while the Love mode vibrates mainly in the horizontal (x) direction. Note that the surface acoustic waves adopted in most applications are the Rayleigh mode [31].

We use a finite-element method in COMSOL to simulate the supported acoustic modes at a wavelength of 2.5 μm (see the Supplemental Material [36]). Figure 2(e) plots the propagation loss of the two acoustic modes in a straight phononic waveguide with $h_{clad} = 700$ nm and $h_{GaN} = 1.4$ μm as a function of the waveguide width w. The propagation loss of the Rayleigh mode remains low, irrespective of the variation of waveguide width, while that of the Love mode depends strongly on the waveguide width and reaches zero periodically. Note that the simulated propagation loss here is induced only by the perfectly matched layer at the simulation boundaries, without considering fabrication imperfections, electrical conductivities, and scattering by thermal phonons. It indicates the confinement capability of the slot waveguide and is usually an underestimate compared with the experimental results [40]. Figure 2(f) plots the simulated frequency of the two acoustic modes as a function of the GaN layer thickness h_{GaN}, with a fixed waveguide width of $w = 9.2$ μm. For the Rayleigh mode, the frequency first decreases and then levels off as h_{GaN} increases. This is because, as shown in the displacement field profiles of the two acoustic modes in the insets of Fig. 2(f), the Rayleigh mode has its displacement field distributed mostly near the GaN layer's upper surface, and the sapphire substrate plays a negligible role in modal confinement at a large GaN layer thickness. Figure 2(g) plots the simulated propagation loss of the two acoustic modes as a function of the GaN layer thickness h_{GaN}, with a fixed waveguide width of $w = 9.2$ μm. The Rayleigh mode maintains a low propagation loss, irrespective of the variation of h_{GaN}. By contrast, the Love mode starts with a high propagation loss, which as h_{GaN} increases first decreases to zero and then increases. Its high propagation loss at h_{GaN} far away from 1.5 μm is attributed to its weak modal confinement and energy leakage to the substrate continuum. Due to the consistently low propagation loss, the Rayleigh
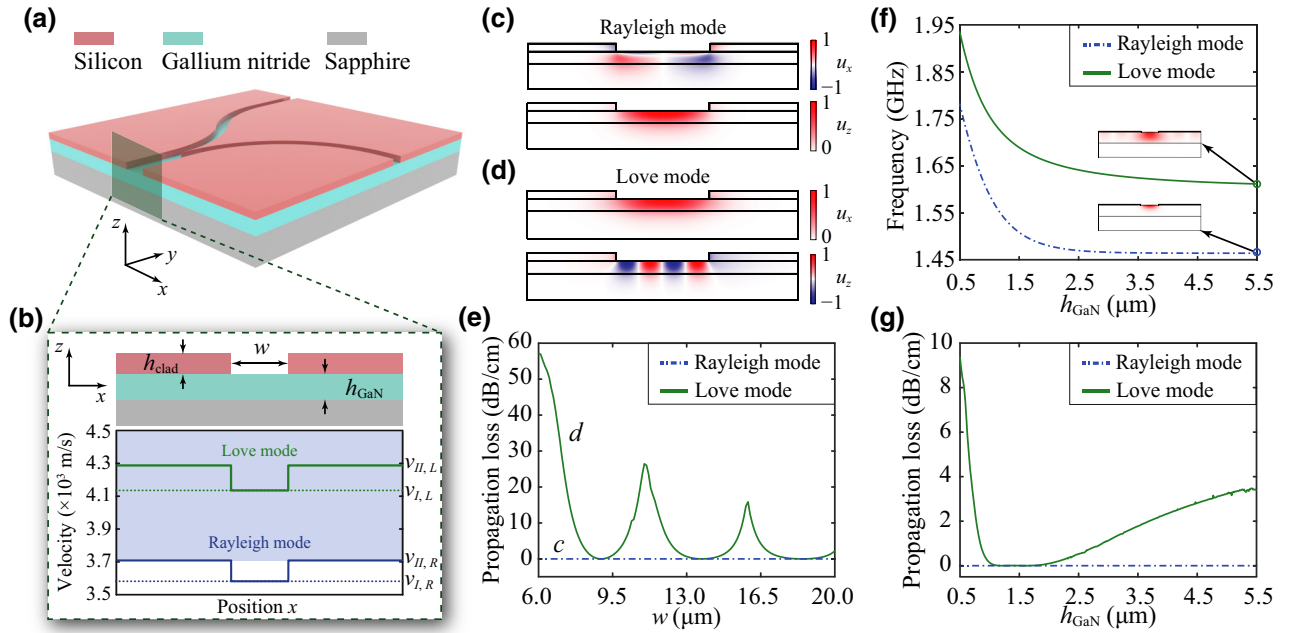
FIG. 2. (a) Conceptual illustration of the proposed overlay slot phononic waveguides for gigahertz phononic integrated circuits. (b) Cross section of the phononic waveguide structure and distribution of effective velocity of the supported acoustic waves. (c),(d) Displacement profiles of the Rayleigh mode (c) and Love mode (d) of the phononic waveguide. (e) Propagation loss as a function of the waveguide width w for the Rayleigh mode and Love mode. (f) Frequency of the propagating acoustic wave as a function of the GaN layer thickness for the Rayleigh mode and Love mode. Insets plot the modal profiles of the Rayleigh mode and Love mode with $h_{GaN} = 5.5$ μm. (g) Propagation loss as a function of the GaN layer thickness for the Rayleigh mode and Love mode. In (b),(f),(g), the waveguide width is $w = 9.2$ μm.

mode is usually adopted in surface-acoustic-wave-based device applications. Next we focus our experiments on demonstrating guiding and routing of the Rayleigh mode by the proposed phononic waveguides.

We fabricate multiple types of devices on a GaN-on-sapphire wafer with $h_{GaN} = 5.2$ μm. Fabrication starts with growth of an epitaxial GaN film on a c-plane sapphire wafer by using metal-organic chemical vapor deposition. Then, we transfer a 700-nm-thick silicon layer from a silicon-on-insulator wafer to the GaN-on-sapphire wafer. Next, we spin coat a layer of electron-beam resist on the silicon-on-GaN-on-sapphire wafer. The pattern of the waveguides is defined by high-resolution electron-beam lithography, and then transferred to the silicon layer by inductively coupled plasma reactive-ion etching. After that, we perform a second step of electron-beam lithography to define the pattern of interdigital transducers (IDTs) with 2.5-μm pitch and 50% duty cycle. The IDTs are fabricated by a lift-off process after depositing stacked layers of titanium (5 nm thick) and gold (40 nm thick) on the patterned electron-beam resist. Here, the waveguide width is chosen to be 7.0 μm such that only the fundamental Rayleigh mode can have good confinement. Figures 3(a) and 3(b) show the fabricated 90°-bend and S-bend devices based on the proposed phononic waveguides, respectively.

Figure 3(c) presents the magnified images showing the details of an IDT.

We first measure a fabricated 90°-bend device as shown in Fig. 3(a). We deliver a sinusoidal rf signal from a vector network analyzer (Keysight E5071C) to the input IDT via a microwave electrical probe (GGB industries), collect the transmitted signal from the output IDT, and send the signal back to the vector network analyzer. The working principle of the IDTs for conversion between rf signals and acoustic waves can be found in the Supplemental Material [36]. The solid line in Fig. 3(d) plots the measured $|S_{21}|$ transmission spectrum in the frequency range of 1.42–1.52 GHz. The observed fringes are attributed to a combined effect of direct electromagnetic radiation (EMR) between the electrical probes and the propagation of acoustic waves. Figure 3(d) inset plots the impulse response in the time domain, where two signals separated by a time delay of 0.288 μs are clearly visible. The first signal is caused by EMR and the second one by the acoustic waves. After a time-gating process and subsequent Fourier transform [41], we obtain the processed $|S_{21}|$ spectrum for the part of the contribution by the acoustic waves, as shown by the dotted line in Fig. 3(d). These experimental results provide clear evidence of guiding and routing of acoustic waves by the phononic waveguide in the 90°-bend device.
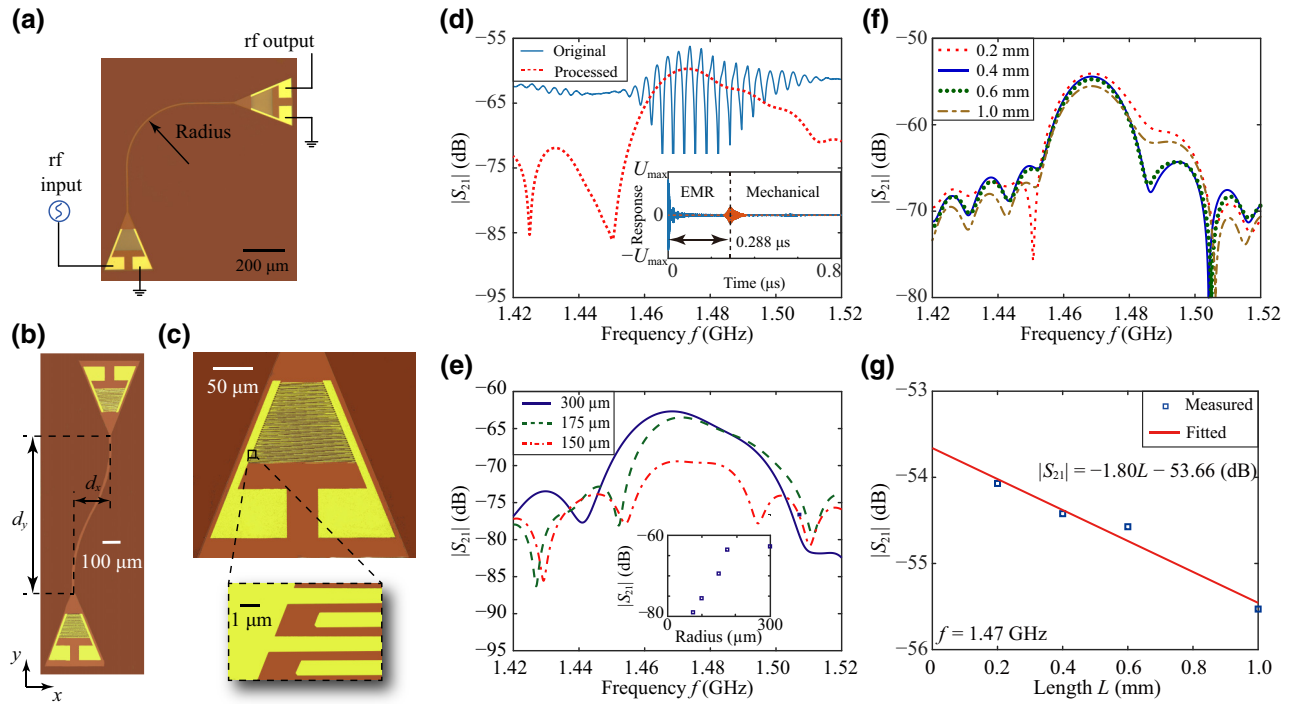
FIG. 3.   (a) Optical microscope image of a fabricated 90°-bend device. (b) Scanning electron microscope image of a fabricated *S*-bend device. (c) Magnified scanning electron microscope images showing details of an interdigital transducer. (d) Originally measured and processed $|S_{21}|$ transmission spectra for a 90°-bend device with a bend radius of 500 μm. Inset plots the measured response in the time domain. (e) Measured $|S_{21}|$ transmission spectra for *S*-bend devices with bend radii of 150, 175, and 300 μm. Inset plots the measured $|S_{21}|$ transmission at an acoustic frequency of 1.47 GHz. (f) Measured $|S_{21}|$ transmission spectra for straight-waveguide devices with waveguide lengths $L = 0.2, 0.4, 0.6$, and 1.0 mm. (g) Measured and fitted $|S_{21}|$ transmission as a function of the waveguide length L at an acoustic frequency of 1.47 GHz.

The phononic waveguide does not introduce additional frequency features in the transmission spectrum. Compared with the $|S_{21}|$ transmission spectra measured from control samples, where two IDTs are fabricated directly on the GaN surface without any waveguide structures (see the Supplemental Material [36]), the $|S_{21}|$ transmission of the 90°-bend devices drops evenly, due to the modal mismatch between the IDT-excited acoustic mode and the waveguide mode.

Next, we measure the acoustic transmission spectra for structures with different bend radii and lengths. Figure 3(b) shows a fabricated *S*-bend device, which consists of a pair of noncollinear IDTs connected by an *S*-bend waveguide. Figure 3(e) plots the measured $|S_{21}|$ transmission spectra for devices with bend radii of 150, 175, and 300 μm. The two IDTs in an *S*-bend device are separated by a distance d_x of 190 μm in the *x* direction and by a distance d_y of 885 μm in the *y* direction. The accumulated bend angle is $2\arccos(1 - d_x/2r)$, with *r* being the bend radius. Clearly, the transmission spectra for the devices with bend radii of 175 and 300 μm are similar, while the device with a bend radius of 150 μm has a much lower transmission. Figure 3(e) inset plots the measured $|S_{21}|$ values as a function of the bend radius at an acoustic frequency of

1.47 GHz, which confirms the effect of the bend radius on the propagation loss. We also measure the $|S_{21}|$ spectra for straight waveguide devices with waveguide lengths of 0.2, 0.4, 0.6, and 1.0 mm and a waveguide width of 7.0 μm; the results are shown in Fig. 3(f) (see the Supplemental Material [36]). Figure 3(g) plots the measured $|S_{21}|$ values at an acoustic frequency of 1.47 GHz for different lengths. The measured $|S_{21}|$ values are linearly fitted as $-1.80L - 53.66$, with a goodness of fit of $R^2 = 0.9684$. Therefore, the measured propagation loss of a straight waveguide is (1.80 ± 0.28) dB/mm, and the additional loss due to electrical impedance mismatch and modal mismatch is about 53.66 dB. With these measured data, we further obtain an intrinsic quality factor (Q_i) of 6064 and an fQ_i product of 8.9×10^{12} Hz. The measured value of propagation loss is larger than its simulated value, due to the additional loss mechanisms, such as air damping, thermal phonon scattering, crystalline defects, and finite electrical conductivities. Nonetheless, our measured propagation loss is comparable to those of suspended phononic waveguides [31] and lithium-niobate-on-sapphire wire waveguides [35]. Based on these experimental results, one can construct a phononic integrated circuit with bends of arbitrary degrees in a more complicated configuration.
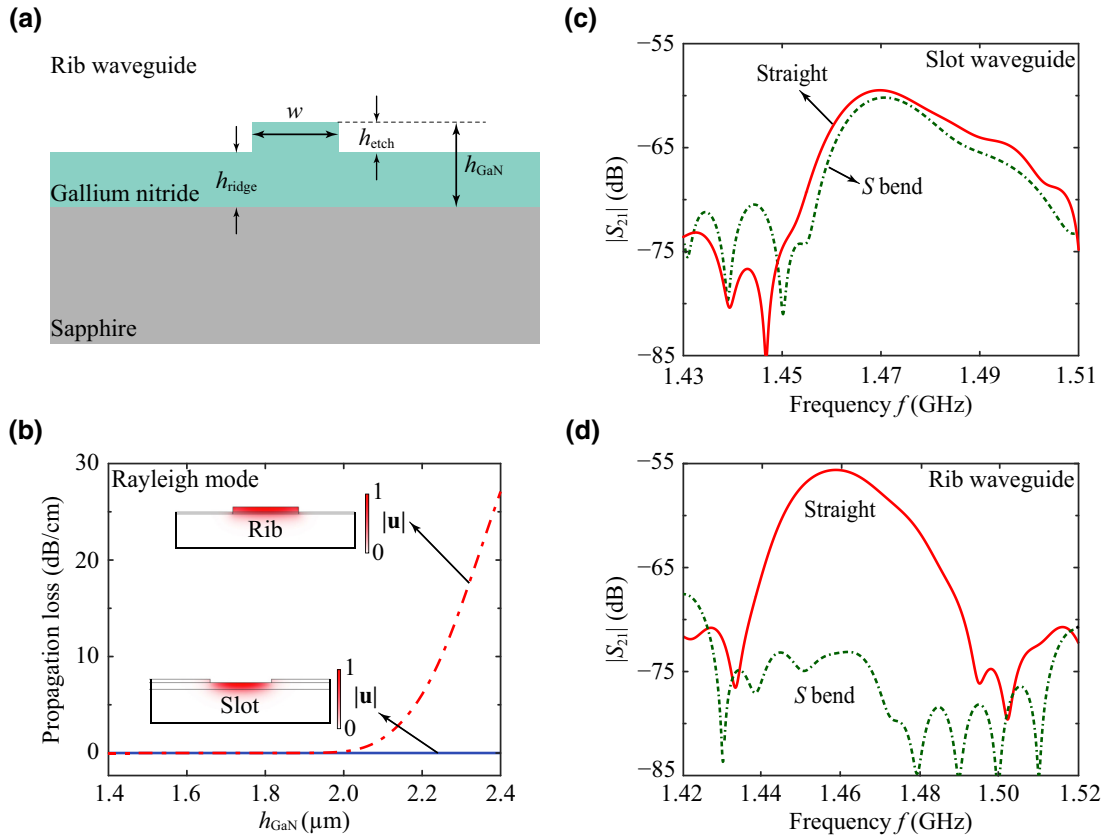
FIG. 4. (a) Cross-sectional illustration of the topographic rib waveguide structure. (b) Rayleigh mode's propagation loss as a function of the GaN layer thickness h_{GaN} for the slot waveguide and rib waveguide with a bend radius of 300 μm. Insets plot the modal profiles of the Rayleigh mode in the two types of phononic waveguides. (c) Measured $|S_{21}|$ transmission spectra for slot-waveguide devices where two IDTs are connected with an S bend or a straight waveguide. (d) Measured $|S_{21}|$ transmission spectra for rib-waveguide devices where two IDTs are connected with an S bend or a straight waveguide.

To demonstrate the advantages of our proposed waveguides in guiding acoustic waves, we compare the performance of our overlay slot waveguide [Fig. 1(d)] and of a rib waveguide [Fig. 1(c)]. As illustrated in Fig. 4(a), a rib waveguide is formed by shallowly etching the GaN layer with an etch depth of h_{etch}, which can also laterally confine and longitudinally guide acoustic waves with compatibility for electronic and photonic integration. By using the finite-element method, we calculate the propagation loss of the two types of waveguides with a bend radius of 300 μm as a function of h_{GaN} under the conditions of $h_{etch} = h_{clad} = 700$ nm; the results are plotted in Fig. 4(b). For the rib waveguide structure, the propagation loss increases as h_{GaN} increases, which is attributed to enhanced dissipation in a thicker GaN ridge layer. For the slot waveguide structure, the propagation loss remains low, irrespective of the variation in h_{GaN}. Therefore, the slot waveguide has advantages over the rib waveguide for substrates with a thick GaN layer. Experimentally, we fabricate on a substrate with $h_{GaN} = 5.2$ μm a straight waveguide with a length of 640 μm and an S bend with a bend radius of 300 μm and accumulated bend angle of

86° for each of the two types of waveguides and measure their $|S_{21}|$ spectra; the results are shown in Figs. 4(c) and 4(d). For structures based on the slot waveguide, the S bend has a similar transmission spectrum to that of the straight waveguide. By contrast, for structures based on the rib waveguide, the S bend has a significantly lower transmission than that of the straight waveguide. It should be noted that the higher transmission measured from the straight rib waveguide is attributed to lower impedance mismatching and modal mismatching during excitation of the acoustic mode in this waveguide. These experimental results clearly show the advantages of slot waveguides over rib waveguides in guiding and transmitting acoustic waves on a chip.

To demonstrate the practicality of the proposed phononic waveguide, we fabricate power splitters which are a commonly used functional component in a phononic integrated circuit. As shown in Fig. 5(a), the power splitter is based on a multimode directional coupler, with its input and output ports connected to IDTs. Figure 5(b) shows the displacement profiles of the fundamental and first-order Rayleigh modes of the multimode phononic waveguide.
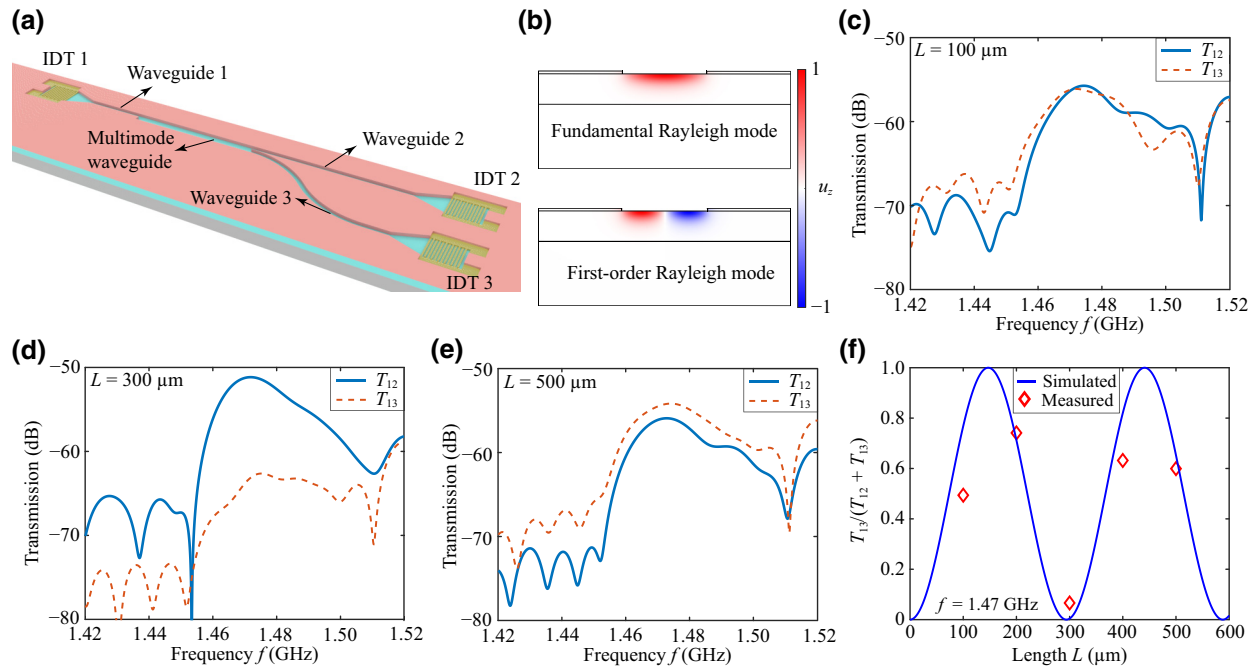
FIG. 5. (a) Illustration of a power splitter based on a multimode directional coupler. (b) Modal profiles of the fundamental and first-order Rayleigh modes for the multimode phononic waveguide. (c)–(e) Measured T_{12} and T_{13} transmission spectra for the multimode waveguide structure with lengths $L = 100$ μm (c), 300 μm (d), and 500 μm (e). (f) Numerically simulated and experimentally measured ratio of acoustic intensities between that at port IDT 3 and the sum of those at ports IDT 2 and IDT 3.

The fundamental and first-order Rayleigh modes propagate at different velocities, and thus the acoustic field in the multimode phononic waveguide varies periodically with the propagation length [42]. In the fabricated device, the acoustic wave excited by IDT 1 first propagates in waveguide 1 with a waveguide width of 7.0 μm, and then enters the multimode waveguide with a waveguide width of 14.7 μm. After propagation through the multimode waveguide, part of the acoustic wave enters waveguide 2 (right branch) and is detected by IDT 2, while the rest enters waveguide 3 (left branch) and is detected by IDT 3. The period for the same acoustic field pattern appearing in the multimode waveguide can be derived from the frequency difference ($2\Delta f$) between the fundamental and first-order Rayleigh modes at a wavelength of 2.5 μm. For the waveguide with a waveguide width of 14.7 μm, the frequencies of the fundamental and first-order modes are 1.4576 and 1.4704 GHz, respectively. The spatial frequency (g) for the varying acoustic pattern can be calculated as 1756 m^{-1} [42]. The acoustic transmittance from waveguide 1 to waveguide 3 varies with the multimode waveguide length L as $\sin^2(2\pi gL)$, and that from waveguide 1 to waveguide 2 varies as $1 - \sin^2(2\pi gL)$. Figures 5(c)–5(e) plot the measured rf transmission spectra T_{12} (from IDT 1 to IDT 2) and T_{13} (from IDT 1 to IDT 3) of the power-splitter devices with $L = 100$, 300, and 500 μm. For devices with $L = 100$ and 500 μm, the transmission spectra T_{12} and T_{13} are quite similar, but for the device with $L = 300$ μm, transmission

T_{12} is much higher than T_{13}. Figure 5(f) plots the simulated and measured ratios of acoustic intensities between T_{13} and $T_{12} + T_{13}$ at a frequency of 1.47 GHz for devices with different L. The theoretical and experimental results agree well with each other.

Finally, we numerically analyze the Love mode of the overlay slot waveguides, which is usually employed for biosensing applications [13]. Figure 6(b) plots the propagation loss of the Love mode propagating in a straight waveguide [Fig. 6(a)] as a function of the waveguide width w and wavelength λ. Clearly, the propagation loss vanishes for certain combinations of w and λ. This is because, under these conditions, the Love mode is decoupled from the high-order Rayleigh modes due to perfect destructive interference between the dissipation channels at the two waveguide edges, exhibiting a phononic analog of the bound state in the continuum (BIC) in a waveguide [43]. Note that such phononic BICs while perfectly confined transversely are still propagating along the longitudinal direction. As shown in Fig. 6(c), the tolerance of the waveguide width for maintaining a propagation loss below 1 dB/cm is 1.0 μm around the desired waveguide width of 9.0 μm. Under the same mechanism, waveguides with a larger width, such as 13.7 and 18.4 μm, can also support the Love mode with a low propagation loss. The tolerance of the waveguide width for maintaining a low propagation loss is even higher, because of enhanced confinement of the acoustic waves in wider waveguides. Figure 6(e) plots
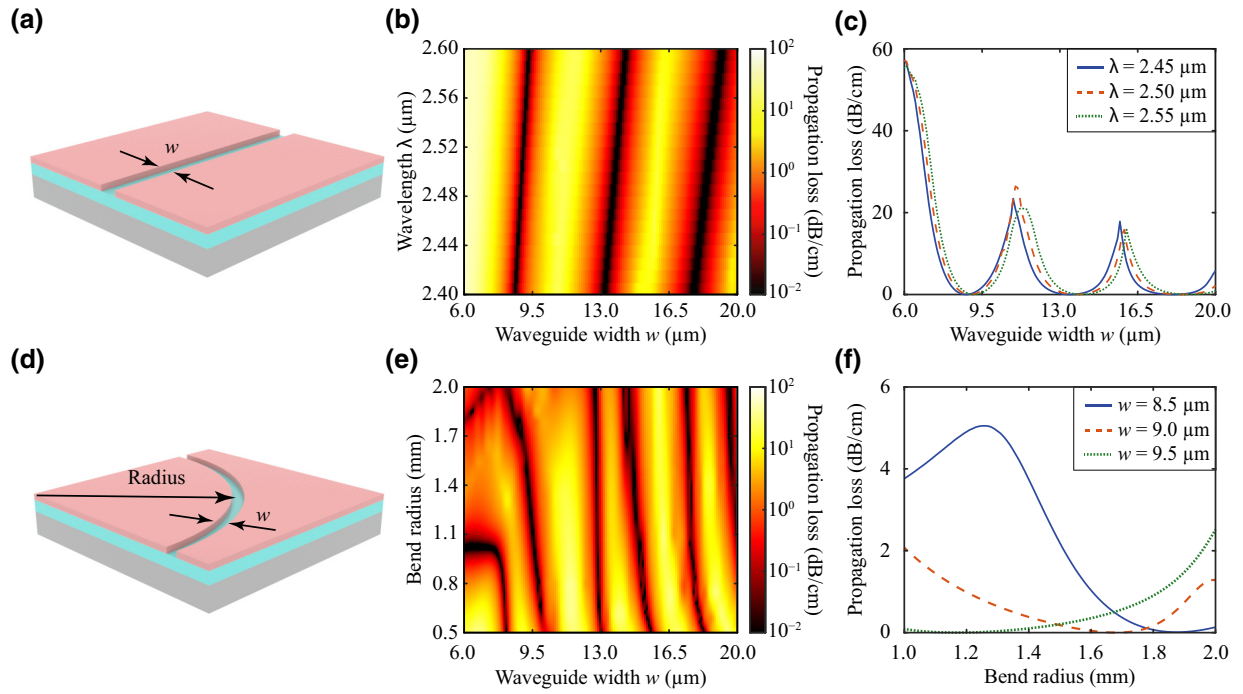
FIG. 6. Numerical results of the Love mode of the overlay slot waveguides. (a) Illustration of a straight waveguide. (b) Propagation loss of the Love mode in the straight waveguide as a function of the waveguide width w and wavelength λ. The propagation loss approaches zero (black regions) for certain combinations of parameters, where the BIC condition is satisfied. (c) Propagation loss as a function of the waveguide width w at wavelengths $\lambda = 2.45$, 2.50, and 2.55 µm. (d) Illustration of a bent waveguide. (e) Propagation loss as a function of the waveguide width w and bend radius at $\lambda = 2.50$ µm. Similar to the straight waveguide, the propagation loss approaches zero (black regions) for certain combinations of parameters, where the BIC condition is satisfied. (f) Propagation loss as a function of the bend radius at $\lambda = 2.50$ µm with $w = 8.5$, 9.0, and 9.5 µm.

the propagation loss of the Love mode propagating in a bent waveguide [Fig. 6(d)] as a function of the waveguide width w and bend radius. Under a similar mechanism as that for the straight waveguide, the propagation loss of a bent waveguide vanishes for certain combinations of w and bend radius. For any bend radius, there are always multiple waveguide widths to achieve the phononic BIC.

III. CONCLUSION

We propose and experimentally demonstrate a type of overlay slot phononic waveguide working at about 1.47 GHz with a propagation loss of 1.80 dB/mm measured in ambient air. Such waveguides have a propagation loss comparable to that of other types of phononic waveguides but with substantially reduced fabrication difficulty. The Rayleigh mode vibrating mainly in the vertical direction can be well confined and guided by these slot waveguides. This strategy can also be adopted for other piezoelectric materials that cannot be grown or deposited on substrates with a high acoustic velocity. We further demonstrate a commonly used functional component in a phononic integrated circuit, power splitters with different splitting ratios, based on multimode directional coupling. Such devices

by manipulating higher-order acoustic modes can be further developed to enhance their information-transmission capacity. Lastly, we point out that, under certain combinations of geometric parameters, the Love mode vibrating mainly in the horizontal direction can become a bound state in the continuum, which adds an additional channel for enhanced capacity of signal transmission and processing. By maintaining a low propagation loss with relaxed technical requirements, the proposed and experimentally demonstrated phononic waveguides will enable alternative ways of information processing and manipulation of biomolecules with phononic integrated circuits on a chip.

[1] M. Aspelmeyer, T. J. Kippenberg, and F. Marquardt, Cavity optomechanics, Rev. Mod. Phys. **86**, 1391 (2014).

[2] K. Jensen, K. Kim, and A. Zettl, An atomic-resolution nanomechanical mass sensor, Nat. Nanotechnol. **3**, 533 (2008).

[3] D. Bothner, S. Yanai, A. Iniguez-Rabago, M. Yuan, Y. M. Blanter, and G. A. Steele, Cavity electromechanics with parametric mechanical driving, Nat. Commun. **11**, 1589 (2020).

[4] J. Zheng, X. Sun, Y. Li, M. Poot, A. Dadgar, N. N. Shi, W. H. P. Pernice, H. X. Tang, and C. W. Wong, Femtogram dispersive *L*3-nanobeam optomechanical cavities: Design and experimental comparison, Opt. Express **20**, 26486 (2012).

[5] X. Sun, J. Zheng, M. Poot, C. W. Wong, and H. X. Tang, Femtogram doubly clamped nanomechanical resonators embedded in a high-*Q* two-dimensional photonic crystal nanocavity, Nano Lett. **12**, 2299 (2012).

[6] M. Sansa, M. Defoort, A. Brenac, M. Hermouet, L. Banniard, A. Fafin, M. Gely, C. Masselon, I. Favero, G. Jourdan, and S. Hentz, Optomechanical mass spectrometry, Nat. Commun. **11**, 3781 (2020).

[7] A. Venkatasubramanian, V. T. K. Sauer, S. K. Roy, M. Xia, D. S. Wishart, and W. K. Hiebert, Nano-optomechanical systems for gas chromatography, Nano Lett. **16**, 6975 (2016).

[8] W. Yu, W. C. Jiang, Q. Lin, and T. Lu, Cavity optomechanical spring sensing of single molecules, Nat. Commun. **7**, 12311 (2016).

[9] D. A. Golter, T. Oo, M. Amezcua, K. A. Stewart, and H. Wang, Optomechanical Quantum Control of a Nitrogen-Vacancy Center in Diamond, Phys. Rev. Lett. **116**, 143602 (2016).

[10] R. Riedinger, S. Hong, R. A. Norte, J. A. Slater, J. Shang, A. G. Krause, V. Anant, M. Aspelmeyer, and S. Gröblacher, Non-classical correlations between single photons and phonons from a mechanical oscillator, Nature **530**, 313 (2016).

[11] L. Lin, R. T. Howe, and A. P. Pisano, Microelectromechanical filters for signal processing, J. Microelectromech. Syst. **7**, 286 (1998).

[12] S. A. Tadesse and M. Li, Sub-optical wavelength acoustic wave modulation of integrated photonic resonators at microwave frequencies, Nat. Commun. **5**, 5402 (2014).

[13] K. Länge, B. E. Rapp, and M. Rapp, Surface acoustic wave biosensors: A review, Anal. Bioanal. Chem. **391**, 1509 (2008).

[14] D. A. Golter, T. Oo, M. Amezcua, I. Lekavicius, K. A. Stewart, and H. Wang, Coupling a Surface Acoustic Wave to an Electron Spin in Diamond via a Dark State, Phys. Rev. X **6**, 041060 (2016).

[15] X. Xi, J. Ma, S. Wan, C.-H. Dong, and X. Sun, Observation of chiral edge states in gapped nanomechanical graphene, Sci. Adv. **7**, eabe1398 (2021).

[16] J. Ma, X. Xi, and X. Sun, Experimental demonstration of dual-band nano-electromechanical valley-Hall topological metamaterials, Adv. Mater. **33**, 2006521 (2021).

[17] H. Wohltjen and R. Dessy, Surface acoustic wave probe for chemical analysis. I. Introduction and instrument description, Anal. Chem. **51**, 1458 (1979).

[18] X. Ding, S.-C. S. Lin, B. Kiraly, H. Yue, S. Li, I. K. Chiang, J. Shi, S. J. Benkovic, and T. J. Huang, On-chip manipulation of single microparticles, cells, and organisms using surface acoustic waves, Proc. Natl. Acad. Sci. U. S. A. **109**, 11105 (2012).

[19] L. Y. Yeo and J. R. Friend, Ultrafast microfluidics using surface acoustic waves, Biomicrofluidics **3**, 012002 (2009).

[20] C. Campbell, *Surface Acoustic Wave Devices and Their Signal Processing Applications* (Elsevier, San Diego, 1989).

[21] K. J. Satzinger, Y. P. Zhong, H.-S. Chang, G. A. Peairs, A. Bienfait, Ming-Han Chou, A. Y. Cleland, C. R. Conner, É. Dumur, J. Grebel, I. Gutierrez, B. H. November, R. G. Povey, S. J. Whiteley, D. D. Awschalom, D. I. Schuster, and A. N. Cleland, Quantum control of surface acoustic-wave phonons, Nature **563**, 661 (2018).

[22] M. M. de Lima, F. Alsina, W. Seidel, and P. V. Santos, Focusing of surface-acoustic-wave fields on (100) GaAs surfaces, J. Appl. Phys. **94**, 7848 (2003).

[23] H. F. Tiersten, Elastic surface waves guided by thin films, J. Appl. Phys. **40**, 770 (1969).

[24] L. R. Adkins and A. J. Hughes, Elastic surface waves guided by thin films: Gold on fused quartz, IEEE Trans. Microwave Theory Tech. **17**, 904 (1969).

[25] A. Khelif, A. Choujaa, S. Benchabane, B. Djafari-Rouhani, and V. Laude, Guiding and bending of acoustic waves in highly confined phononic crystal waveguides, Appl. Phys. Lett. **84**, 4400 (2004).

[26] J.-H. Sun and T.-T. Wu, Propagation of surface acoustic waves through sharply bent two-dimensional phononic crystal waveguides using a finite-difference time-domain method, Phys. Rev. B **74**, 174305 (2006).

[27] Y. Wang, J. Lee, X.-Q. Zheng, Y. Xie, and P. X. L. Feng, Hexagonal boron nitride phononic crystal waveguides, ACS Photonics **6**, 3225 (2019).

[28] M. Kurosu, D. Hatanaka, and H. Yamaguchi, Mechanical Kerr Nonlinearity of Wave Propagation in an On-Chip Nanoelectromechanical Waveguide, Phys. Rev. Appl. **13**, 014056 (2020).

[29] E. Romero, R. Kalra, N. P. Mauranyapin, C. G. Baker, C. Meng, and W. P. Bowen, Propagation and Imaging of Mechanical Waves in a Highly Stressed Single-Mode Acoustic Waveguide, Phys. Rev. Appl. **11**, 064035 (2019).

[30] Q. Liu, H. Li, and M. Li, Electromechanical Brillouin scattering in integrated optomechanical waveguides, Optica **6**, 778 (2019).

[31] Y. D. Dahmani, C. J. Sarabalis, W. Jiang, F. M. Mayor, and A. H. Safavi-Naeini, Piezoelectric Transduction of a Wavelength-Scale Mechanical Waveguide, Phys. Rev. Appl. **13**, 024069 (2020).

[32] W. Fu, Z. Shen, Y. Xu, C.-L. Zou, R. Cheng, X. Han, and H. X. Tang, Phononic integrated circuitry and spin–orbit interaction of phonons, Nat. Commun. **10**, 2743 (2019).

[33] M. Bicer, S. Valle, J. Brown, M. Kuball, and K. C. Balram, Gallium nitride phononic integrated circuits platform for GHz frequency acoustic wave devices, Appl. Phys. Lett. **120**, 243502 (2022).

[34] X.-B. Xu, X.-B. Xu, J.-Q. Wang, Y.-H. Yang, W. Wang, Y.-L. Zhang, B.-Z. Wang, C.-H. Dong, L. Sun, G.-C. Guo, C.-L. Zou, High-frequency traveling-wave phononic cavity

with sub-micron wavelength, Appl. Phys. Lett. **120,** 163503 (2022).

[35] F. M. Mayor, W. Jiang, C. J. Sarabalis, T. P. McKenna, J. D. Witmer, and A. H. Safavi-Naeini, Gigahertz Phononic Integrated Circuits on Thin-Film Lithium Niobate on Sapphire, Phys. Rev. Appl. **15,** 014039 (2021).

[36] See the Supplemental Material http://link.aps.org/supplemental/10.1103/PhysRevApplied.19.064076 for additional information, which includes Refs. [37–39].

[37] D. Royer and E. Dieulesaint, *Elastic Waves in Solids II: Generation, Acousto-optic Interaction, Applications* (Springer Science & Business Media, New York, 1999).

[38] E. A. Kittlaus, W. M. Jones, P. T. Rakich, N. T. Otterstrom, R. E. Muller, and M. Rais-Zadeh, Electrically driven acousto-optics and broadband non-reciprocity in silicon photonics, Nat. Photonics **15,** 43 (2021).

[39] A. F. Wright, Elastic properties of zinc-blende and wurtzite AlN, GaN, and InN, J. Appl. Phys. **82,** 2833 (1997).

[40] L. Shao, S. Maity, L. Zheng, L. Wu, A. Shams-Ansari, Y.-I. Sohn, E. Puma, M.N. Gadalla, M. Zhang, C. Wang, E. Hu, K. Lai, and M. Lončar, Phononic Band Structure Engineering for High-Q Gigahertz Surface Acoustic Wave Resonators on Lithium Niobate, Phys. Rev. Appl. **12,** 014022 (2019).

[41] I. S. Camara, B. Croset, L. Largeau, P. Rovillain, L. Thevenard, and J. Y. Duquesne, Vector network analyzer measurement of the amplitude of an electrically excited surface acoustic wave and validation by x-ray diffraction, J. Appl. Phys. **121,** 044503 (2017).

[42] P. A. Besse, M. Bachmann, H. Melchior, L. B. Soldano, and M. K. Smit, Optical bandwidth and fabrication tolerances of multimode interference couplers, J. Lightwave Technol. **12,** 1004 (1994).

[43] Z. Yu, X. Xi, J. Ma, H. K. Tsang, C.-L. Zou, and X. Sun, Photonic integrated circuits with bound states in the continuum, Optica **6,** 1342 (2019).